Effects of chemical doping and pressure on $CaFe_4As_3$

Liang L. Zhao,[1] S. K. Kim,[2,3] Gregory T. McCandless,[4] Milton S. Torikachvili,[5] P. C. Canfield,[2,3] Julia Y. Chan,[4] and E. Morosan[1]

[1]*Department of Physics and Astronomy, Rice University, Houston, Texas 77005, USA*
[2]*Department of Physics and Astronomy, Iowa State University, Ames, Iowa 50011, USA*
[3]*Ames Laboratory, US Department of Energy (DOE), Iowa State University, Ames, Iowa 50011, USA*
[4]*Department of Chemistry, Louisiana State University, Baton Rouge, Louisiana 70803, USA*
[5]*Department of Physics, San Diego State University, San Diego, California 92182, USA*

(Received 7 June 2011; revised manuscript received 9 August 2011; published 28 September 2011)

The effects of chemical doping by P, Yb, Co, and Cu, and hydrostatic pressure on $CaFe_4As_3$, were studied on single-crystalline samples. While the former two dopants substitute the nonmagnetic ions, the latter two partially occupy the Fe sites within the magnetic sublattice. The incommensurate spin density wave (IC-SDW) ordering at $T_N \sim 88$ K in $CaFe_4As_3$ changes only by up to ~40% with doping and applied pressure. Thus the IC-SDW state appears more robust than in the layered Fe pnictides. The commensurate SDW (C-SDW) state below $T_2 \sim 26$ K is suppressed in the Co-doped series, while it moves up in temperature in the P-, Yb-, and Cu-doped compounds. A new magnetic phase transition is observed at an intermediate temperature T_3 in $Ca(Fe_{1-x}Co_x)_4As_3$. Resistivity and magnetization measurements on $CaFe_4As_3$ were performed under hydrostatic pressure up to 5 GPa, showing a systematic decrease of T_N and a domelike phase boundary at T_2 up to $p_c \sim 2.10$ GPa. At higher pressures, a possible structural phase transition occurs, marked by a slowly increasing transition temperature. A phase diagram is shown to compare the effects of chemical doping and pressure.

DOI: 10.1103/PhysRevB.84.104444 PACS number(s): 75.30.Fv, 75.30.Kz, 72.15.−v, 61.50.Ks

I. INTRODUCTION

Transition metal pnictides and chalcogenides have been the focus of intense research in recent years, mainly due to the discovery of superconductivity in such layered compounds.[1–16] Although the superconductivity mechanism in these systems is still not fully understood, the correlations between crystal structure, magnetism, and superconductivity have been widely recognized and studied. Various experiments have shown that the As–Fe–As bond angle,[17,18] the pnictogen height with respect to the plane of Fe sublattice,[19,20] or an orthorhombic distortion in some cases[21] are correlated with the superconductivity temperature T_c. In light of this correlation between crystal structure and physical properties, synthesizing and examining systems with structural similarity to the iron pnictides appears to be a promising avenue for the discovery of novel superconductors.

Recently, a new iron pnictide compound $CaFe_4As_3$ ("143") with complex crystallographic and magnetic structure was reported.[22–24] Different from the layered iron pnictide superconductors, $CaFe_4As_3$ crystallizes with a unique three-dimensional network structure as shown in Fig. 1. In this orthorhombic structure, FeAs tetrahedra form infinitely long ribbons parallel to the b axis. These ribbons are connected by fivefold coordinated Fe^{1+} [labeled Fe(4)] sites, forming channels which host the Ca atoms. The local crystallographic coordination of the other three Fe^{2+} sites [labeled Fe(1-3)] is similar to that in the $FeAs_4$ tetrahedra in the layered iron pnictides. A second-order, incommensurate spin density wave (IC-SDW) transition at $T_N = 88$ K is observed in all thermodynamic measurements on single crystals of $CaFe_4As_3$,[23] similar to the magnetic ordering in the layered undoped iron pnictides. Another similarity with the parent compounds of the iron pnictide superconductors consists in the poor metal properties observed above T_N.[1,23,25] However, unlike in the layered Fe-pnictides, no structural transition is associated with the magnetic ordering in $CaFe_4As_3$,[23,26] possibly because of the already reduced, orthorhombic symmetry in the latter compound. One more distinct feature in the "143" iron arsenide is the first-order transition at $T_2 = 26.4$ K, in which neutron diffraction has shown to be an incommensurate-to-commensurate (IC-C) SDW transition.[26,37] Band-structure calculations indicate that the SDW transition is related to the magnetic instability as a result of Fermi surface nesting, while a first-principles total energy calculation lends support to the scenario of local magnetism in which the IC-SDW order originates from the competing second- and third-nearest-neighbor couplings in the Fe sublattice.[26]

Chemical doping[4,6,27–31] and hydrostatic pressure[32–36] are often employed to suppress the antiferromagnetic (AFM) order in favor of superconductivity. The similarities in structural and physical properties of $CaFe_4As_3$ and the layered iron pnictides, together with the more profound differences between these compounds, motivated the current detailed investigation of the relationship between crystal structure and magnetic and transport properties of $CaFe_4As_3$. Consequently, for the current study we are presenting data on doped $CaFe_4As_3$ single crystals, as well as pressure effects on the transport and magnetization properties of the pure compound. In the former case, we have studied the effects of partial substitutions on each of the three types of atoms in the $CaFe_4As_3$ unit cell, namely, Yb and P doping on the Ca and As sites, respectively, or Co and Cu doping in place of Fe. As will be shown below, the different dopants have drastically distinct effects on the thermodynamic and transport properties, depending on whether charge carriers and disorder are introduced in the magnetic sublattice (as is the case for transition metal doping), or just disorder or chemical pressure (as expected for Yb and P doping).

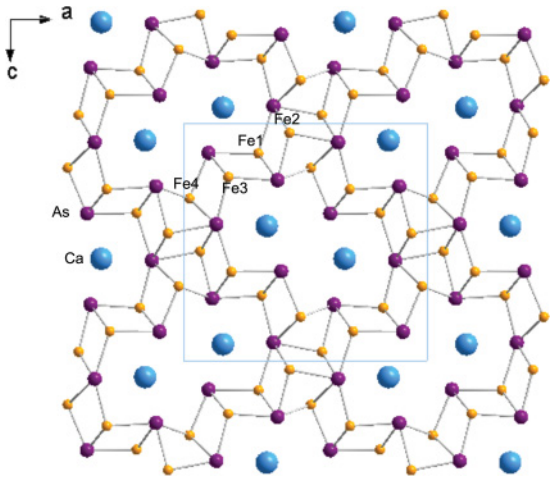

FIG. 1. (Color online) Crystal structure of $CaFe_4As_3$ viewed along the b axis, with the Ca, Fe, and As atoms represented by blue (large), orange (small), and purple (medium) spheres. The four crystallographic Fe sites are labeled. Fe(4) is fivefold coordinated, while Fe(1-3) sites are fourfold coordinated with neighboring As sites.

II. EXPERIMENTAL METHODS

Single crystals of pure and doped $CaFe_4As_3$ have been synthesized using the flux method, similar to our previous report.[23] We have successfully synthesized single crystals of $CaFe_4(As_{1-x}P_x)_3$ ($0 \leqslant x \leqslant 0.25$), $Ca(Fe_{1-x}T_x)_4As_3$ ($0 \leqslant x \leqslant 0.60$ for T = Co, $x = 0.25$ for T = Cu), as well as $Ca_{1-x}Yb_xFe_4As_3$ ($x = 0.2$); all x values are nominal compositions, and estimates of the actual dopant content are discussed below. Attempts to grow single crystals with higher doping levels failed, which suggests that the solubility limit for the "1-4-3" structure may have been reached. The as-grown crystals have rodlike shape with cross sections typically around 1 mm^2, the length of the rods ranging from 3 to 8 mm. Room-temperature powder x-ray diffraction (XRD) measurements were performed on a Rigaku D/Max diffractometer, confirming that all doped crystals are phase pure and isostructural to the undoped $CaFe_4As_3$ compound. No detectable tin peaks were observed in the XRD patterns.

Additional single-crystal XRD experiments were performed, with data collected at room temperature on a Nonius KappaCCD x-ray diffractometer with Mo K_α radiation source ($\lambda = 0.71073$ Å) and graphite monochromator. Single crystals with a low crystal mosaicity ($\sim 0.4^\circ$) were selected from each sample batch and mounted on the tips of thin glass fibers with epoxy. Data were collected at a lower symmetry (monoclinic, $2/m$) than the previously reported crystal system (orthorhombic), and intensities were recorded at a crystal-to-detector distance of 30 mm, between a 2θ angle of 2.5° and 60°. All of the data collections had the same list of suggested systematic absences ($h00{:}h = 2n$, $0k0{:}k = 2n$, $00l{:}l = 2n$, $hk0{:}h = 2n$, $0kl{:}k + l = 2n$, $hh0{:}h = 2n$), lattice type (Primitive), and Laue symmetry (mmm). Structure determinations were made using WINGX[38] with SIR97[39] and SHELXL-97.[40] PLATON[41] was also used to check for missed symmetry (ADDSYM option). Our best models of the x-ray diffraction data are refined with the orthorhombic space group $Pnma$ (no. 62).

Chemical analysis was perform on an FEI Quanta 200 scanning electron microscope (SEM) with an energy-dispersive x-ray (EDX) spectrometer. The measurements were carried out on the same single crystals used for the physical property measurements, and the concentration of each element was determined. Each crystal was scanned at four areas per crystal for 50 seconds per area, with an accelerating voltage of 20 kV and a beam-to-sample distance of 15 mm. The average composition was normalized with the Ca site.

Heat capacity was measured in $H = 0$ in a Quantum Design Physical Property Measurement System (QD PPMS) using the thermal relaxation technique. Temperature-dependent magnetization was measured using the Reciprocating Sample Option (RSO) of a Quantum Design Magnetic Property Measurement System (QD MPMS). The samples were cooled from room temperature to 2 K in zero field. Data up to 300 K were taken on warming in a $H = 0.1$ T field applied along the crystallographic b axis. Magnetization measurements under pressure up to $\sim$0.86 GPa were performed in a QD MPMS using a commercial, Be-Cu, HMD pressure cell. Daphne 7373 oil was used as a pressure medium, and susceptibility of elemental Pb (measured in 20 Oe field) served to determine the pressure in the cell at low temperature. Special attention was paid to have a low and reproducible remanent field in the superconducting magnet for the Pb measurements. Sample measurements were performed for $H = 0.1$ T on warming. The magnetization measurements under pressure were impeded by the several parasitic features. A low-temperature Curie-like tail and broad steplike feature between 100 and 150 K were associated with the magnetic properties of the particular batch of the commercial Be-Cu pistons, and a small susceptibility feature around 10 K was probably caused by the sample, since it was present in the initial run under ambient pressure. However, the sharpness of the two intrinsic transitions at T_N and T_2 (as discussed below) and the relative flatness of the magnetic response of the cell between 20 and 100 K allowed us to follow these transitions under pressure, and assert the absence of the T_3 transition up to 0.86 GPa. Sharp features in the derivatives dM/dT were used to identify the phase transition temperatures T_N and T_2.

DC resistivity measurements were performed in a QD PPMS using a standard four-probe method, with current flowing along the b axis. In addition, AC resistivity of the undoped crystal was measured under pressure up to 2 GPa in a Be-Cu piston-cylinder cell with a center core of tungsten carbide. The sample, manganin, and Pb manometers were inserted in a polytetrafluoroethylene (PTFE) cup containing a 60 : 40 mixture of n-pentane and light mineral oil, which served as the pressure-transmitting medium. Pressure was applied at ambient temperature with a hydraulic press, using the manganin as a high-temperature reference manometer. The pressure was locked in and the cell was then loaded into a QD PPMS, which provided the temperature environment, as well as the electronics, for the resistivity measurements, manometers, and a calibrated Cernox sensor attached to the body of the cell. The pressure at low temperatures was determined from the superconducting transition temperature T_c of the Pb manometer. The cooling and warming rates were kept below 0.3 K/min, which yielded a temperature lag

TABLE I. Lattice parameters and unit cell volume for $CaFe_4(As,P)_3$ and $(Ca_{1-x}Yb_x)Fe_4As_3$.

Dopant		P			Yb
x (nominal)	0	0.05	0.1	0.25	0.2
x (EDX)	0	Crystal 1	Crystal 2	Crystal 3	0.17
a (Å)	11.919(3)	11.917(3)	11.915(5)	11.911(2)	11.910(2)
b (Å)	3.749(1)	3.748(1)	3.746(2)	3.746(1)	3.748(1)
c (Å)	11.624(3)	11.622(4)	11.619(5)	11.617(2)	11.617(3)
V (Å^3)	519.3(2)	519.1(3)	518.6(4)	518.3(2)	518.6(2)

between the sample and Cernox sensor below 0.5 K at high temperatures and below 0.1 K for $T < 70$ K.

AC resistivity measurements under pressure above 2 GPa were done using a Be-Cu Bridgman anvil cell with tungsten carbide anvils[42] that was modified to work with liquid pressure media.[43] The cell was designed to fit inside a QD PPMS where all pressure measurements were done. The liquid pressure medium used with this cell is a 1:1 mixture of iso-pentane and *n*-pentane, which provided nearly hydrostatic pressure conditions throughout the experiment, as the medium remains liquid up to 6.5 GPa at room temperature.[44] The pressure in the cell was again determined from the T_c of a Pb manometer that had been placed within the sample space. For the highest pressure measurement (5.0 GPa), the Pb manometer was no longer viable below 109 K due to a broken contact. In that case, the room-temperature resistance of the manometer was used for extrapolation based on the known resistivity behavior of lead. As a check, this method was applied to the lower pressure measurements taken in the same set and was found to have the error around 0.1 GPa. Typically, the width of the Pb transition was 0.015 K, which corresponds to a pressure difference of 3.7×10^{-5} GPa at 0 GPa and 4.5×10^{-3} GPa at 5 GPa. For all measurements done with the Bridgman cell, the temperature was lowered from 300 to 30 K at a rate of 1 K/min and raised from 100 to 300 K at 0.5 K/min. From the base temperature to 100 K, the rate of warming was typically 0.2 K/min to minimize the difference between the QD PPMS thermometer reading and the sample space temperature. At this slow warming rate, this difference is less than 100 mK. In temperature regions around the features in resistivity of the sample and manometer, measurements were taken either by stabilizing the temperature at each interval or by ramping the temperature at the lowest rate allowed by the QD PPMS in order to avoid any shifts in temperature. Two sets of measurements were done with the Bridgman anvil cell. The first one (Bridgman cell 1) showed erratic behavior above 100 K due to a crack in the sample. However, the evolution of the transition under pressure was consistent with other data sets; therefore the low-temperature (less than 100 K) data are included in the figures.

III. RESULTS AND DISCUSSION

A. Doping in the nonmagnetic sublattice: $CaFe_4(As_{1-x}P_x)_3$ and $(Ca_{1-x}Yb_x)Fe_4As_3$

P substitutes the isovalent As ions without introducing extra charge carriers. The size difference between the two pnictogens renders the P doping equivalent to applying a positive pressure on the lattice. Single-crystal XRD data (Table I) reveal a very small, albeit systematic, decrease of lattice parameters with increasing nominal P concentration x. The unit cell volume shrinks with increasing x by up to 0.2%, even though EDX analysis indicates that the P concentration is below the instrument's level of detection (typically 5–10%). Based on these results and the changes in the physical properties discussed below, it can be concluded that the actual P content in the doped crystals is finite but much lower than the nominal one. For this reason, we refer to the P-doped samples as $CaFe_4(As,P)_3$ (crystal 1, 2, and 3).

Figure 2 shows the temperature-dependent magnetic susceptibility of pure and P-doped $CaFe_4As_3$ single crystals, measured with $H = 0.1$ T field applied along the b axis. An antiferromagnetic peak in the susceptibility, which has been shown to be a second-order SDW transition in the pure $CaFe_4As_3$,[26,37] can be observed for the undoped sample (black symbols) at $T_N = 88$ K. In the doped samples (crystals 1, 2, and 3), this transition is slowly suppressed, such that the minimum T_N for the P-doped crystals is around 83 K (blue symbols). This decrease of T_N with doping is possibly related to the reduction of Fermi surface nesting that drives the SDW order. Surprisingly, above T_N the susceptibility of both the undoped and P-doped crystals exhibits nearly linear temperature

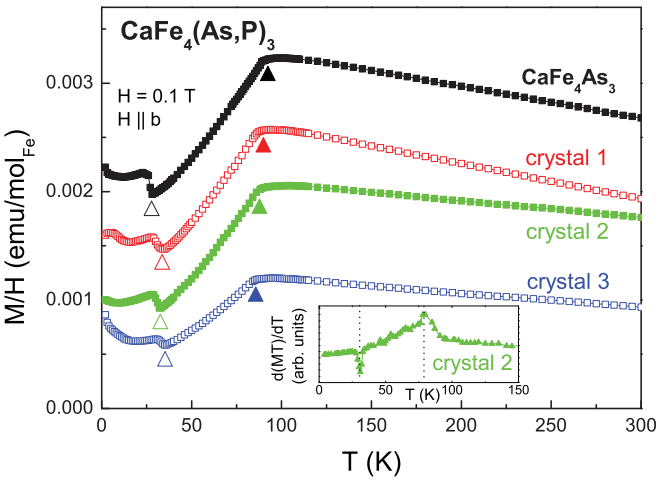

FIG. 2. (Color online) Magnetic susceptibility of $CaFe_4(As,P)_3$ crystals for $H = 0.1$ T and $H \| b$. The $M/H(T)$ curves of the doped compounds have been shifted by –0.0008 emu/mol$_{Fe}$ for clarity. The magnetic transition temperatures T_N and T_2 are marked by solid and open triangles, respectively. Inset: $d(MT)/dT$ data of crystal 2, where T_N and T_2 are marked by vertical lines.

dependence. This non-Curie-Weiss behavior is reminiscent of the normal state susceptibilities of $LaFeAsO_{1-x}F_x$[45] and undoped AFe_2As_2 (A = Ca, Sr, Ba),[46–49] where positive linear temperature dependence above the Néel temperature was observed. Recent theoretical studies[50,51] pointed out that local AFM correlations existing above T_N may be responsible for this unconventional behavior. More similar to the result of $CaFe_4As_3$, the susceptibilities of cuprates $La_{2-x}Sr_xCuO_4$ and $Ba_2Sr_2CuO_{6+\delta}$ display a negative linear temperature dependence above T_N in the overdoped regime, which is proposed to be the result of a van Hove singularity in the density of states near the Fermi surface, in addition to other complex many-body effects such as quasiparticle decay.[52] The origin of this linear temperature dependence observed in the undoped and P-doped $CaFe_4As_3$ crystals still remains unclear, which calls for a careful examination of the band structure and Fermi surface topology. This is left for a future study.

The IC-C SDW transition can be observed as a local minimum in the magnetization of the P-doped samples (Fig. 2). The corresponding temperature T_2, marked by open triangles, increases up to 33 K compared to the value of 26 K in the pure $CaFe_4As_3$ crystals, suggesting that the commensurate SDW structure becomes stable over a wider temperature range as a result of P doping.

The temperature-dependent resistivity data of $CaFe_4As_3$ and $CaFe_4(As,P)_3$ crystals are plotted in Fig. 3. Above T_N the resistivity shows a typical metallic behavior with a weak temperature dependence and room-temperature values around $0.2 - 0.4$ mΩ cm. A local minimum in resistivity (right inset, Fig. 3) can be observed at T_N as a result of the reduced density of states at the Fermi surface associated with the SDW gap. As the temperature is lowered through T_2, a steep drop in resistivity is associated with the IC-C SDW transition, indicating the loss of scattering associated with the phase degree of freedom in the IC-SDW state. The resistivity around T_2 exhibits a large temperature hysteresis [about 4–10 K; left inset, Fig. 3], consistent with the first-order nature of the IC-C SDW transition. It is worth noting that P doping results in a lower residual resistivity ratio $RRR = \rho(300\text{ K})/\rho(2\text{ K})$ than that of the undoped sample. This is likely due to the disorder in the Fe-Pn ribbons (but not the magnetic sublattice itself), which enhances scattering, especially at low temperatures.

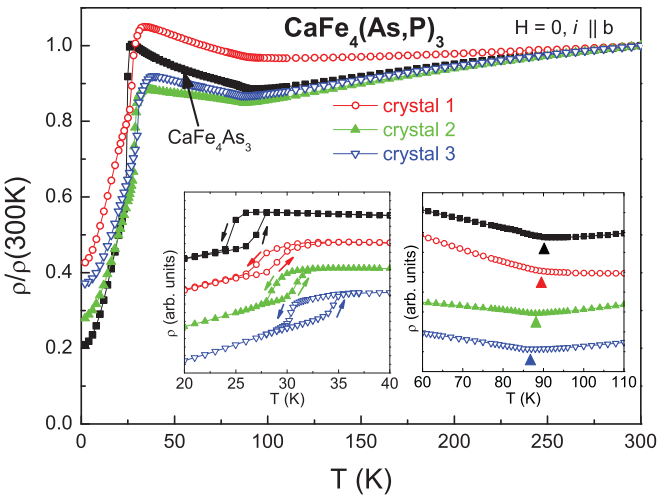

FIG. 3. (Color online) DC resistivity of $CaFe_4As_3$ and $CaFe_4(As,P)_3$ crystals for $H = 0$ and $i \| b$. The data were taken during cooling and scaled by the resistivity at 300 K. Inset (left): an expanded view around the IC-C SDW transition at T_2, showing curves measured during both cooling and warming. Inset (right): an expanded view around the SDW transition, with T_N marked by solid triangles.

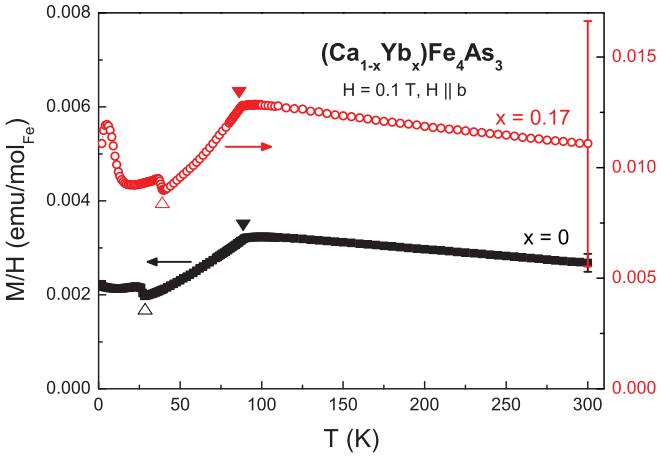

FIG. 4. (Color online) Magnetic susceptibility of $(Ca_{1-x}Yb_x)Fe_4As_3$ crystals ($x = 0$ and 0.17) for $H = 0.1$ T and $H \| b$. The transition temperatures T_N and T_2 are marked by solid and open triangles, respectively. The large error bar in magnetization for $x = 0.17$ (red symbols) is due to the very small mass (∼0.1 mg) of the crystal.

Similar to P doping, chemical pressure may also be achieved via Yb doping. As a result of the close ionic radii of Yb^{2+} (∼1.08 Å) and Ca^{2+} (∼1.09 Å) ions,[53] the Yb dopant is most likely to occupy the Ca sites, in which case the Fe-As sublattice remains ordered. The Yb concentration determined by EDX measurements is ∼0.17, fairly consistent with the nominal x value given the detection limit of EDX (5–10%). Single-crystal XRD data for $(Ca_{1-x}Yb_x)Fe_4As_3$ (Table I) indicate that the unit cell volume decreases only by 0.13% for the doped sample. Such a minute volume change is consistent with the small difference between the ionic radii of Yb^{2+} and Ca^{2+}.

Figure 4 shows the magnetic susceptibility of undoped $CaFe_4As_3$ and $Ca_{0.83}Yb_{0.17}Fe_4As_3$, measured in an applied field $H = 0.1$ T along the crystallographic b axis. Just like for P doping, both features at T_N and T_2 are preserved in the Yb-doped crystal. As x increases, the SDW transition (solid triangles, Fig. 4) moves to slightly lower temperature while T_2 (open triangles, Fig. 4) exhibits a more significant increase from 26.4 to 38 K. These changes are also reflected in the scaled resistivity data (Fig. 5), in which the transport behavior of undoped and doped samples is almost identical, except for the shift in critical temperatures and the resistivity drop at T_2. For the doped sample (open symbols, Fig. 4), an additional peak at 5 K in the magnetic susceptibility suggests the system may undergo another phase transition at low temperatures, although any corresponding feature is obscured in the resistivity data down to 2 K. It is not clear whether this transition is intrinsic to the compound, since a very small amount of magnetic impurity, though not detectable in the x-ray data, may also induce this peak. The origin of this feature calls for a detailed study of the low-temperature

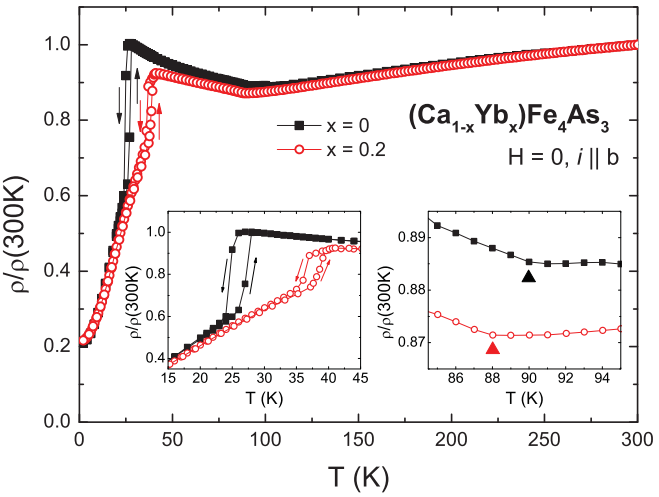

FIG. 5. (Color online) DC resistivity of $(Ca_{1-x}Yb_x)Fe_4As_3$ crystals ($x = 0$ and 0.17) for $H = 0$ and $i \| b$. The data were taken during both cooling and warming, and were scaled by the resistivity at 300 K. Inset (left): an expanded view around the IC-C SDW transition at T_2. Inset (right): an expanded view around the SDW transition, with T_N marked by solid triangles.

magnetic structure by means of neutron diffraction, and this is the subject of an ongoing investigation.

B. Doping in the magnetic sublattice: $Ca(Fe_{1-x}T_x)_4As_3$, T = Co and Cu

The results of EDX and single-crystal XRD measurements on $Ca(Fe_{1-x}Co_x)_4As_3$ crystals are shown in Table II. According to the EDX analysis, the Co content x of the doped samples (listed in Table II) is close to half of the nominal value for $x_{nominal} > 0.1$. XRD data indicate that all the lattice parameters decrease systematically with increasing Co concentration and the unit cell volume shrinks by 1.2% from $x = 0$ to 0.32. Additionally, a comparison of the Fe–As bond lengths in the $x = 0$ and 0.32 compounds (Table III) shows a larger change of the Fe(1-3)–As than the Fe(4)–As bond lengths. This suggests that Co selectively occupies the Fe(1-3) sites first. By contrast, Cr was shown to preferentially occupy the Fe(4) site.[54]

The magnetic susceptibility of $Ca(Fe_{1-x}Co_x)_4As_3$ as a function of temperature for $H = 0.1$ T and $H \| b$ is plotted in Fig. 6(a). The SDW ordering, marked by solid triangles, exhibits a systematic shift to lower temperatures as the dopant amount x increases. Similar to the P-doped crystals, a non-Curie-Weiss linear temperature dependence can be observed

TABLE III. Fe–As bond lengths d in $Ca(Fe_{1-x}Co_x)_4As_3$ ($x = 0$ and 0.32) and $\Delta d = d(x = 0.32) - d(x = 0)$.

Bond	Bond length d (Å)		
	$x = 0$	$x = 0.32$	Δd (Å)
Fe(1)–As(1)	2.4434(8)	2.4206(10)	−0.0228(18)
Fe(1)–As(2)	2.4677(6)	2.4410(7)	−0.0267(13)
Fe(1)–As(3)	2.4359(8)	2.4049(10)	−0.0310(18)
Fe(2)–As(1)	2.4343(6)	2.3882(10)	−0.0461(16)
Fe(2)–As(1)	2.4245(9)	2.3961(7)	−0.0284(16)
Fe(2)–As(2)	2.3920(8)	2.3619(11)	−0.0301(19)
Fe(3)–As(1)	2.3854(8)	2.3681(11)	−0.0173(19)
Fe(3)–As(2)	2.4191(9)	2.3932(11)	−0.0259(20)
Fe(3)–As(3)	2.4139(6)	2.4030(7)	−0.0109(13)
Fe(4)–As(1)	2.6122(6)	2.6169(7)	0.0047(13)
Fe(4)–As(2)	2.5787(6)	2.5790(7)	0.0003(13)
Fe(4)–As(3)	2.4328(8)	2.4141(11)	−0.0187(19)

in the susceptibility above T_N. In the samples with $x \leqslant 0.1$, the IC-C SDW transition broadens and moves down in temperature with increasing x. For $x > 0.1$, no sign of this transition can be traced down to 2 K. Though qualitatively different from the results of P doping, the strong suppression of the IC-C SDW transition in Co-doped $CaFe_4As_3$ is not unexpected. The SDW order develops within the magnetic sublattice consisting of moment-bearing Fe ions. The magnetization data suggest that Co doping on the magnetic Fe sublattice results in a stronger perturbation of the C-SDW compared to the case of the substitution of As with P (Fig. 2). This could be a result of Co inducing disorder, or introducing extra charge carriers, or both. Such scenarios are indeed consistent with the resistivity behavior as shown in Fig. 7. The scaled resistivity $\rho/\rho(300\ K)$ is nearly independent of the Fe-Co ratio above T_N, and the resistivity minimum at T_N moves down in temperature by only 15% up to $x = 0.32$. As soon as Co is introduced in the system ($x = 0.05$, red symbols, Fig. 7), the residual resistivity ρ_0 is three times larger than for the undoped crystals (black symbols, Fig. 7) and the sharp drop at T_2 disappears. Instead, the doped samples display only a broad local maximum below T_N, which broadens further and nearly disappears as ρ_0 increases with increasing x.

However, a new magnetic phase transition [marked by open triangles in Fig. 6(a)] is observed in the $M(T)$ data for the $x \geqslant 0.1$ samples at an intermediate temperature T_3 between T_N and T_2, manifested as a peak in $d(MT)/dT$ for $x \geqslant 0.1$ [Fig. 6(b)]. While a peak at T_3 in the heat capacity data [as exemplified in

TABLE II. Lattice parameters and unit cell volume of $Ca(Fe_{1-x}Co_x)_4As_3$ and $Ca(Fe,Cu)_4As_3$ crystals.

Dopant		Co						Cu
x (nominal)	0	0.05	0.1	0.2	0.3	0.4	0.6	0.25
x (EDX)	0	0.05	0.07	0.1	0.16	0.2	0.32	(see text)
a (Å)	11.919(3)	11.917(2)	11.914(4)	11.907(2)	11.902(2)	11.897(2)	11.878(2)	11.919(3)
b (Å)	3.749(1)	3.750(1)	3.749(1)	3.748(1)	3.748(1)	3.747(1)	3.745(1)	3.751(1)
c (Å)	11.624(3)	11.618(2)	11.611(4)	11.600(2)	11.587(3)	11.571(3)	11.533(2)	11.623(3)
V (Å^3)	519.3(2)	519.1(2)	518.6(2)	517.6(2)	516.9(1)	515.8(1)	513.0(2)	519.6(2)

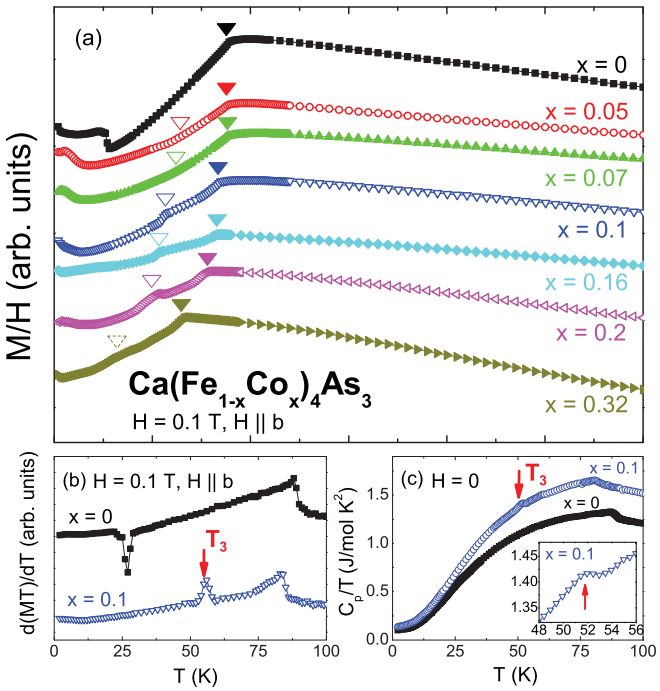

FIG. 6. (Color online) (a) Magnetic susceptibility of $Ca(Fe_{1-x}Co_x)_4As_3$ crystals ($x = 0$, 0.05, 0.07, 0.1, 0.16, 0.2, and 0.32) for $H = 0.1$ T and $H\|b$. The curves for the doped samples have been shifted along the vertical axis for clarity. Solid and open triangles mark the positions for T_N and T_3, respectively. (b) $d(MT)/dT$ for $H\|b$ and $x = 0$ and 0.1, illustrating how the transition temperature T_3 is determined for $x \geqslant 0.1$. (c) C_p/T for $x = 0$ and 0.1, with T_3 marked by a red arrow; inset: a zoomed-in view of the transition at T_3 for $x = 0.1$.

Fig. 6(c) for $x = 0.1$] confirms this to be a bulk transition, it is, however, obscured in the $\rho(T)$ data by the broader maximum below T_N and by the increasing ρ_0 relative to $\rho(300\ \mathrm{K})$.

One possible scenario for explaining the T_3 transition is a spin reorientation that leads to a different magnetic state below T_3 compared to the C-SDW state below T_2. Another scenario to be considered is that if Co is also magnetic, as is the case in many Co compounds, the Fe and Co magnetic moments order at different temperatures, T_N and T_3, respectively. In this case the decrease of the Fe composition with increasing x would be consistent with the decreasing T_N. However, one would expect T_3 to move up with increasing x if the Co ions ordered independently at this intermediate temperature. The simultaneous decrease of T_N and T_3 with x is an indication that Fe and Co magnetic moments are coupled. Neutron diffraction experiments on the Co-doped samples are underway, and they may elucidate the nature of the transitions in $Ca(Fe_{1-x}Co_x)_4As_3$.

By comparison with the isovalent P-As and Yb-Ca substitutions, the results of Co doping demonstrate that substituting transition metal atoms for Fe casts more significant changes on the magnetic structure of $CaFe_4As_3$ system. This is possibly due to the two different moment-carrying ions. It would be useful to compare the dopings we presented so far with the effect of nonmagnetic substitution on the Fe sublattice. If Cu had a 1+ oxidation state when doped into $CaFe_4As_3$, it may provide such an opportunity, together with the likely

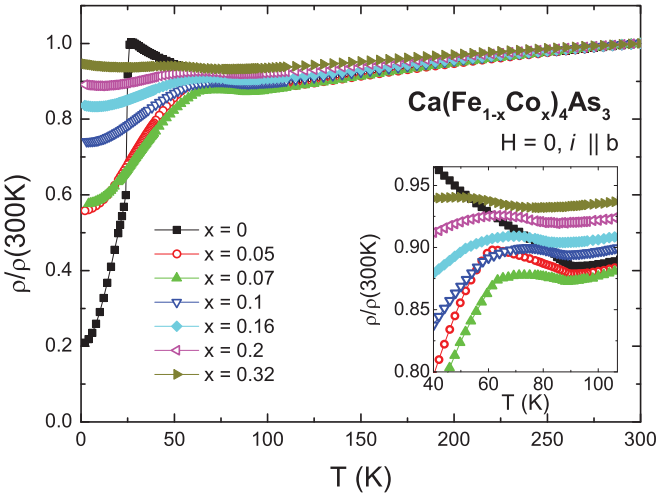

FIG. 7. (Color online) DC resistivity data for $Ca(Fe_{1-x}Co_x)_4As_3$ crystals ($x = 0$, 0.05, 0.07, 0.1, 0.16, 0.2, and 0.32) for $H = 0$ and $i\|b$, scaled at $T = 300$ K. Inset: an expanded view of the scaled resistivity values near T_N.

scenario that it would preferentially substitute on the Fe^{1+} sites only. The $BaFe_2As_2$ system serves as a good example[55] for the versatility of transition metal doping, in which both Co and Cu doping suppress the structural phase transition and SDW ordering. However, the former one stabilizes the superconducting phase in a wide range of x values, while no superconductivity is observed in the latter case.

As seen in Fig. 8, the magnetic susceptibility of $Ca(Fe,Cu)_4As_3$ shows obvious differences compared to the Co-doped series (Figs. 6 and 7). The IC-C SDW transition

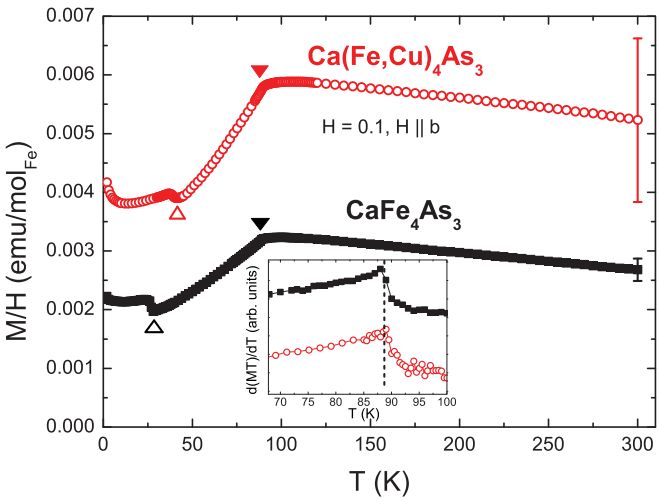

FIG. 8. (Color online) Magnetic susceptibility of $Ca(Fe,Cu)_4As_3$ crystals for $H = 0.1$ T and $H\|b$. Full and open triangles mark the position of the SDW ordering temperature T_N and the IC-C SDW transition at T_2, respectively. The large error bar in magnetization for the doped compound (red symbols) is due to the very small mass (~0.4 mg) of the crystal measured. Inset: An expanded view of $d(MT)/dT$ near T_N. The values have been rescaled and shifted along the vertical axis for clarity. The dotted line marks the peak position in $d(MT)/dT$, which shows no change from the undoped to the doped compound.

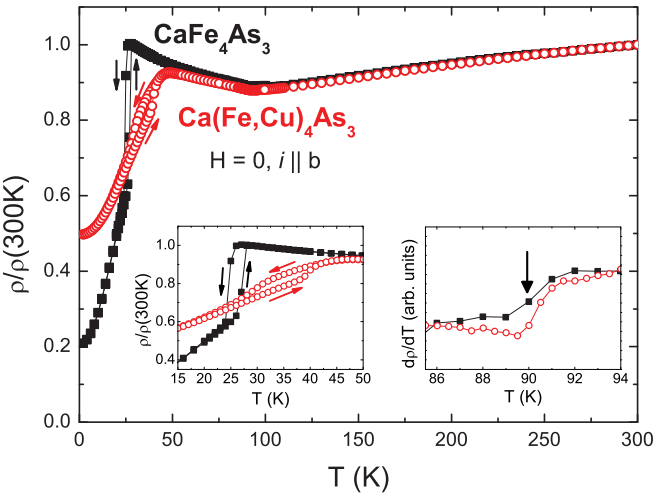

FIG. 9. (Color online) DC resistivity of $CaFe_4As_3$ and $Ca(Fe,Cu)_4As_3$ crystals for $H = 0$ and $i \| b$, measured on both cooling and warming. Inset (left): an expanded view of the resistivity around T_2. Inset (right): an expanded view of $d\rho/dT$ around T_N, for which the maximum slope is associated with the transition (vertical arrow).

is preserved in the Cu-doped sample, with T_2 moving up to ~40 K (red symbols, Fig. 8). Surprisingly, T_N experiences almost no change (inset, Fig. 8). By contrast, in the Co-doped series, a dopant concentration of $x = 0.1$ was already high enough to move T_N down by 4.5 K (5%) and to suppress the IC-C SDW transition below 2 K. The robustness of the SDW order against Cu doping suggests that the topology of the Fermi surface is much less perturbed in this case than in the case of other dopants. A further assumption supported by this robust SDW ordering is the selective site occupation for Cu, similar to the case of Cr doping in a previous report.[54] If Cu^{1+} (the most stable oxidation state of Cu) preferentially occupies the Fe(4) sites first, no extra charge carrier will be introduced into the system until all the Fe^{1+} ions on Fe(4) sites are replaced by Cu^{1+}. Consequently, for $x \leqslant 0.25$ the Fermi surface is less likely to encounter a drastic change, which is favorable for a stable SDW order. While the unaltered T_N in the Cu-doped sample is justified in this scenario, the T_2 increase can be simply understood as a pressure-tuning effect. Determined from single-crystal XRD measurements, the unit cell volume for the Cu-doped sample is slightly larger than for the undoped one, indicating a negative chemical pressure that may be responsible for the observed change in T_2.

The resistivity of $Ca(Fe,Cu)_4As_3$ shown in Fig. 9 is in good agreement with the magnetization data. Above 45 K the scaled resistivity data for both undoped and doped samples are almost identical. When the temperature is lowered below 45 K, the resistivity of the doped sample starts to decrease as a result of the IC-C SDW transition. However, unlike the abrupt drop observed in the pure system, the feature around T_2 becomes broader and smoother in the doped crystals (left inset, Fig. 9), especially on cooling. It is remarkable, however, that the drop in ρ(T) associated with the IC-C SDW transition is smaller and the residual resistivity more than double compared to the undoped sample. It is reasonable to assume that some disorder is still induced by Cu doping, even in the selective doping picture. EDX results indicate that the actual Cu content is much less than the nominal value $x = 0.25$, in which case Cu and Fe ions are mixed on the Fe(4) sites.

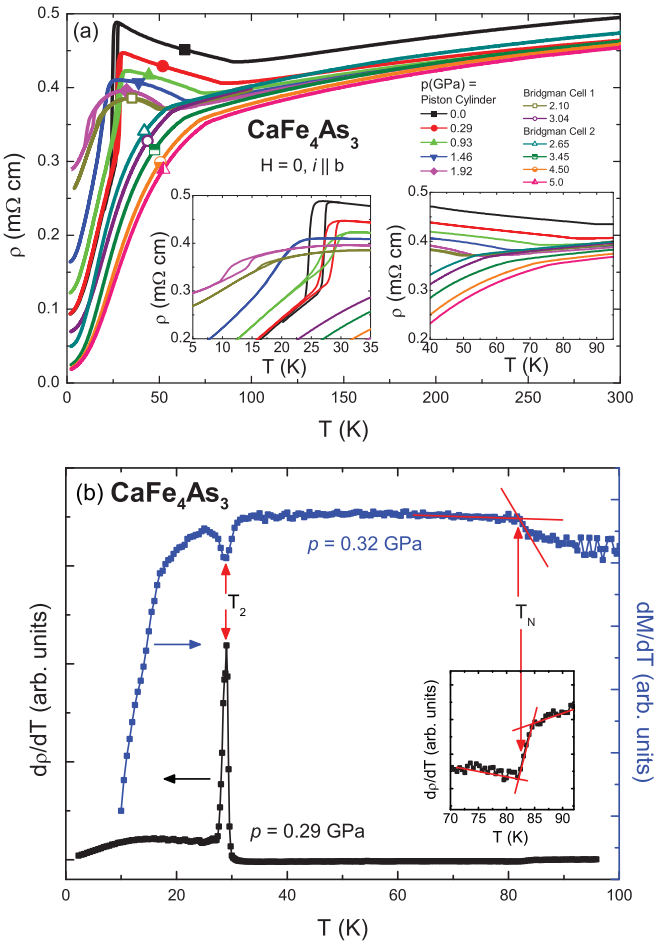

FIG. 10. (Color online) (a) AC resistivity of $CaFe_4As_3$ for $H = 0$ and $i \| b$, measured under pressure varying from 0 to 5 GPa. Insets: expanded view of the resistivity near T_2 (left) and T_N (right). (b) Examples of how the transition temperatures were determined (vertical arrows) from $d\rho/dT$ (left axis) and dM/dT (right axis). Inset: expanded view of $d\rho/dT$ around T_N.

C. Effects of hydrostatic pressure

Figure 10(a) shows the AC resistivity of $CaFe_4As_3$ samples measured under pressure. For low-pressure measurements performed with the piston cylinder (full symbols), as pressure increases, T_N decreases at a rate of –18.5 K/GPa until it reaches a minimum at around 53 K (right inset, Fig. 10). Simultaneously, T_2 first moves up to a maximum of around 30 K at 0.93 GPa (light green curve), then drops to 14 K with pressures up to 1.92 GPa (left inset, Fig. 10). These results show good consistency with the data on P-doped crystals, in which substituting As with smaller P ions can be viewed as positive chemical pressure. The fact that T_2 moves up in the P-doped $CaFe_4As_3$ suggests that the chemical pressure equivalent to this maximum P composition is smaller than 0.93 GPa, which also maximizes T_2. It is also worth noting that the drop of resistivity near T_2 becomes less abrupt as pressure increases and eventually evolves into a smooth, domelike feature at 1.92 GPa. This change in resistivity

behavior suggests that the C-SDW is destabilized by increasing pressure above 1.92 GPa.

For higher pressures, the sample for the first set of measurements done with the Bridgman anvil cells (cell 1) had a partial crack, which led to erratic resistance readings above 100 K. However, the low-temperature data from these measurements provide qualitative results linking the low- and high-pressure resistivity behaviors. As can be seen in Fig. 10, the lowest pressure curve with the Bridgman cell 1 at 2.10 GPa (dark yellow) shows the same domelike low-temperature behavior as the highest piston cylinder cell measurement (magenta). For pressure above 2.65 GPa, the transition at T_2 is no longer visible and the local maximum at T_N disappears, replaced by a drop in resistivity. It is not clear whether the state below this transition is still SDW; thus the transition temperature is labeled T^* instead of T_N, to distinguish from the SDW ordering temperature for the low-pressure regime. Overall, the resistivity drops with increasing hydrostatic pressure, suggesting that the crystals become more metallic. This was predicted[57] as one necessary condition for the occurrence of superconductivity in $CaFe_4As_3$. However, the qualitative change in the resistivity behavior between $p = 2.10$ and 2.65 GPa may be associated with a structural phase transition. In this case, other means for increasing the metallicity in $CaFe_4As_3$ should be tested as avenues for superconductivity. Future pressure-dependent x-ray diffraction measurements will be performed to verify the presence of a structural phase transition in $CaFe_4As_3$.

Another sample in a Bridgman cell (cell 2) was prepared and measured under pressure values $p = 2.65 - 5.0$ GPa. At 3.45 GPa, low ramping rate measurements were done on warming and cooling across T^* and no hysteretic behavior was found. Increasing the pressure caused an increase of T^* at a rate of 9.4 K/GPa. The nature of this transition needs to be investigated once the structural phase transition is confirmed or not by pressure x-ray experiments. Independent of whether a structural distortion is associated with the qualitative change in $\rho(T)$ at $p = 2.65$ GPa, it is not clear whether the SDW order is preserved at higher pressures.

Magnetization measurements under pressure were also performed on $CaFe_4As_3$ for pressures up to 0.86 GPa. The two transition temperatures observed in the resistivity data are indeed confirmed by the magnetization measurements: a jump in dM/dT is observed around T_N [right axis, Fig. 10(b)], while a local minimum is associated with the IC-C SDW transition [left axis, Fig. 10(b)].

IV. DISCUSSION AND CONCLUSIONS

A doping (x) and hydrostatic pressure (p) study was performed on single crystals of $CaFe_4As_3$. The two tuning parameters $\mathcal{C} = x$ or p can have similar effects on the crystal structure by decreasing the unit cell volume. Additionally, doping can induce disorder, expand the lattice, add charge carriers, or modify the magnetic structure.

For a comparison between the doping and pressure effects, the transition temperatures in the T - $\mathcal{C}$ phase diagram (Fig. 11) are plotted as a function of $\mathcal{C} = \Delta V$ or p, where $\Delta V = V$(pure crystal)–V(doped crystal) is the change in volume for the doped samples relative to that of pure $CaFe_4As_3$. As can

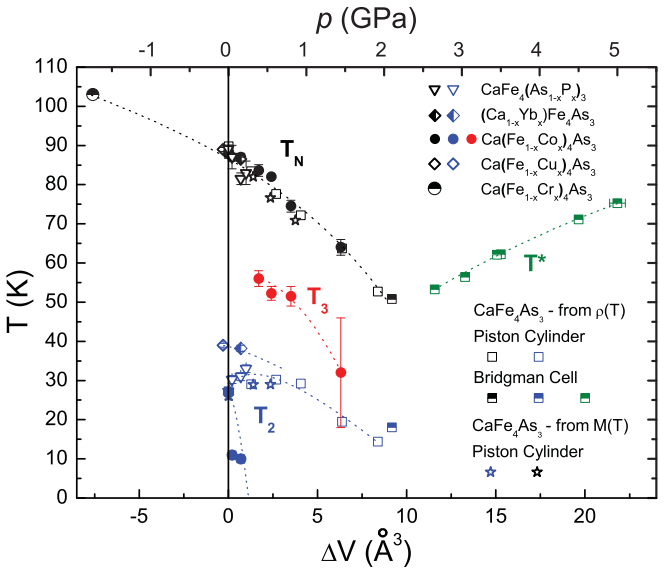

FIG. 11. (Color online) T - $\mathcal{C}$ phase diagram of $CaFe_4As_3$, with $\mathcal{C}$ = change in volume [see text] (bottom axis) or pressure (top axis). The transition temperatures T_N, T_2, T_3, and T^* are shown in black, blue, red, and green, respectively. Points determined from resistivity pressure data collected with a piston cylinder and Bridgman cell are marked by open and half-filled squares, respectively, and those from magnetization measurements under pressure are shown as open stars. The results on doped samples are marked by open triangles (P), half-filled diamonds (Yb), solid circles (Co), and open diamonds (Cu). The point for $CaCr_{0.84}Fe_{3.16}As_3$ (half-filled circle, Ref. 54) is also plotted in the phase diagram, showing good consistency with the dependence of T_N on ΔV observed in our data. Dotted and dashed lines are guides to the eye for possible phase boundaries.

be seen in the phase diagram in Fig. 11, the SDW ordering temperature T_N (black symbols) decreases with both ΔV and p up to critical values $\Delta V_c \sim 10$ Å^3 and $p_c \sim 2$ GPa. A remarkable similarity between the ΔV and p dependence of T_N is apparent from the black symbols in the phase diagram in Fig. 11. From this coincidence, a bulk modulus $\kappa = -V(\partial p/\partial V)$ can be determined to be $\kappa \simeq 119$ GPa, comparable to the value of 71 GPa for $BaFe_2As_2$.[56]

For pressures above p_c, a phase transition is still visible (green symbols); however, it moves up in temperature as p increases to 5 GPa. At p_c, a qualitative change in the $\rho(T)$ data is observed in Fig. 10(a), from a local minimum to an inflection point for $p < p_c$ and $p > p_c$, respectively. This suggests a possible structural change at p_c, in which case the transition at higher pressures (dashed line in Fig. 11) may correspond to a magnetic ordering, distinct from the SDW at ambient pressure. According to the prediction[57] that the increase in metallicity in $CaFe_4As_3$ may lead to a superconducting (SC) ground state, pressures higher than 5 GPa are needed to reach the SC state. X-ray diffraction measurements under pressure will verify the existence of the structural phase transition around 2 GPa, and this is left to a future study.

The behavior of the IC-C SDW transition (blue symbols in Fig. 11) varies more with the type of tuning parameters. A smaller drop in resistivity at T_2 is observed upon P, Yb, and Cu substitutions (Figs. 3, 5, and 9, respectively). The initial increase of T_2 with pressure (open blue squares and

stars, Fig. 11) is consistent with the observed behavior when smaller P ions partially replace As ions (open blue triangles, Fig. 11). Yb and Cu substitutions (diamonds) increase T_2 faster compared to P doping or pressure, while an increase in pressure between 0.5 and 2 GPa slowly reduces T_2. Interestingly, for $p = 2.10$ GPa, the lower temperature transition seen in resistivity (blue, half-filled square, Fig. 11) appears close to the extrapolated phase boundaries at both T_3 (dotted red line, Fig. 11) and T_2 (dotted blue line, Fig. 11). The type of this transition remains unknown and can be either one of the two.

A distinct behavior in both magnetization (Fig. 6) and resistivity (Fig. 7) is induced by Co doping. On one hand, the low-temperature transition T_2 is quickly suppressed by $x < 0.1$, as seen in the magnetization data. An additional transition occurs in the doped samples with $x \geqslant 0.1$ at T_3 [open triangles in Fig. 6(a)] and increasing amounts of Co reduce this transition temperature. However, Co substitution obscures the two low-temperature transitions T_2 and T_3 in the resistivity data, while determining the residual resistivity ratio RRR to decrease with x (Fig. 7). Despite the similarities in the structural changes, P, Yb, and Co have different effects on the physical properties. The former two substitute for the nonmagnetic, isoelectronic As and Ca ions, respectively. The latter dopant, however, is smaller in size, carries a magnetic moment, and has an extra d electron compared to the Fe^{2+} that it substitutes for. It is not surprising then that different types of changes are observed for the magnetic transitions. Cu doping is structurally different from the other three substitutions, as it appears to expand the unit cell volume. However, the physical properties resemble those seen in the case of the non-magnetic dopants P and Yb, where T_N changes little with x, and the T_2 IC-C SDW transition moves up in temperature. At the same time, Cu doping is distinct from the Co substitution on the magnetic sublattice, suggesting that Cu may be non-magnetic when doped into $CaFe_4As_3$.

In conclusion, a very robust SDW ordering is observed in $CaFe_4As_3$, with little change in T_N by either doping or pressure. A lower IC-C SDW transition associated with Fermi surface nesting is, however, greatly affected by the different tuning parameters. The resistivity values remain relatively high, characteristic of poor metals. Improving the metallicity may lead to either superconductivity or good thermal electric properties in this three-dimensional iron pnictide compound.

ACKNOWLEDGMENTS

The authors thank S. L. Bud'ko for carrying out magnetization measurements under pressure. Work at Rice University was supported by AFOSR-MURI. The research performed at the Ames Laboratory was supported by the US Department of Energy, Office of Basic Energy Science, Division of Materials Sciences and Engineering. Ames Laboratory is operated for the US Department of Energy by Iowa State University under Contract No. DE-AC02-07CH11358. Work at LSU was partially supported by NSF DMR-0756281. Work at San Diego State University was supported by NSF DMR-0805335.

[1] Y. Kamihara, T. Watanabe, M. Hirano, and H. Hosono, J. Am. Chem. Soc. **130**, 3296 (2008).
[2] G. F. Chen, Z. Li, D. Wu, G. Li, W. Z. Hu, J. Dong, P. Zheng, J. L. Luo, and N. L. Wang, Phys. Rev. Lett. **100**, 247002 (2008).
[3] Z. A. Ren, J. Yang, W. Lu, W. Yi, G. C. Che, X. L. Dong, L. L. Sun, and Z. X. Zhao, Mater. Res. Innovations **12**, 105 (2008).
[4] Z.-A. Ren, J. Yang, W. Lu, W. Yi, X.-L. Shen, Z.-C. Li, G.-C. Che, X.-L. Dong, L.-L. Sun, F. Zhou, and Z.-X. Zhao, Europhys. Lett. **82**, 57002 (2008).
[5] Z.-A. Ren, W. Lu, J. Yang, W. Yi, X.-L. Shen, Z.-C. Li, G.-C. Che, X.-L. Dong, L.-L. Sun, F. Zhou, and Z.-X. Zhao, Chin. Phys. Lett. **25**, 2215 (2008).
[6] P. Cheng, L. Fang, H. Yang, X. Zhu, G. Mu, H. Luo, Z. Wang, and H. H. Wen, Sci. China G **51**, 719 (2008).
[7] J.-W. G. Bos, G. B. S. Penny, J. A. Rodgers, D. A. Sokolov, A. D. Huxley, and J. P. Attfield, Chem. Commun. 3634 (2008).
[8] M. Rotter, M. Tegel, and D. Johrendt, Phys. Rev. Lett. **101**, 107006 (2008).
[9] K. Sasmal, B. Lv, B. Lorenz, A. M. Guloy, F. Chen, Y.-Y. Xue, and C.-W. Chu, Phys. Rev. Lett. **101**, 107007 (2008).
[10] A. S. Sefat, R. Jin, M. A. McGuire, B. C. Sales, D. J. Singh, and D. Mandrus, Phys. Rev. Lett. **101**, 117004 (2008).
[11] X. C. Wang, Q. Q. Liu, Y. X. Lv, W. B. Gao, L. X. Yang, R. C. Yu, F. Y. Li, and C. Q. Jin, Solid. State. Commun. **148**, 538 (2008).
[12] D. R. Parker, M. J. Pitcher, P. J. Baker, I. Franke, T. Lancaster, S. J. Blundell, and S. J. Clarke, Chem. Commun. 2189 (2009).
[13] F.-C. Hsu, J.-Y. Luo, K.-W. Yeh, T.-K. Chen, T.-W. Huang, P. M. Wu, Y.-C. Lee, Y.-L. Huang, Y.-Y. Chu, D.-C. Yan, and M.-K. Wu, Proc. Nat. Acad. Sci. **105**, 14262 (2008).
[14] K.-W. Yeh, T.-W. Huang, Y.-L. Huang, T.-K. Chen, F.-C. Hsu, P. M. Wu, Y.-C. Lee, Y.-Y. Chu, C.-L. Chen, J.-Y. Luo, D.-C. Yan, and M.-K. Wu, Europhys. Lett. **84**, 37002 (2008).
[15] H. Ogino, Y. Matsumura, Y. Katsura, K. Ushiyama, S. Horii, K. Kishio, and J Shimoyama, Supercond. Sci. Technol. **22**, 075008 (2009).
[16] H. Ogino, K. Machida, A. Yamamoto, K. Kishio, J. Shimoyama, T. Tohei, and Y. Ikuhara, Supercond. Sci. Technol. **23**, 115005 (2010).
[17] C.-H. Lee, A. Iyo, H. Eisaki, H. Kito, M. T. Fernandez-Diaz, T. Ito, K. Kihou, H. Matsuhata, M. Braden, and K. Yamada, J. Phys. Soc. Jpn. **77**, 083704 (2008).
[18] J. Zhao, Q. Huang, C. de la Cruz, S. Li, J. W. Lynn, Y. Chen, M. A. Green, G. F. Chen, G. Li, Z. Li, J. L. Luo, N. L. Wang, and P. Dai, Nat. Mater. **7**, 953 (2008).
[19] Y. Mizuguchi, Y. Hara, K. Deguchi, S. Tsuda, T. Yamaguchi, K. Takeda, H. Kotegawa, H. Tou, and Y. Takano, Supercond. Sci. Technol. **23**, 054013 (2010).
[20] H. Okabe, N. Takeshita, K. Horigane, T. Muranaka, and J. Akimitsu, Phys. Rev. B **81**, 205119 (2010).
[21] S. Nandi, M. G. Kim, A. Kreyssig, R. M. Fernandes, D. K. Pratt, A. Thaler, N. Ni, S. L. Bud'ko, P. C. Canfield, J. Schmalian, R. J. McQueeney, and A. I. Goldman, Phys. Rev. Lett. **104**, 057006 (2010).

[22]I. Todorov, D. Y. Chung, C. D. Malliakas, Q. Li, T. Bakas, A. Douvalis, G. Trimarchi, K. Gray, J. F. Mitchell, A. J. Freeman, and M. G. Kanatzidis, J. Am. Chem. Soc. **131**, 5405 (2009).
[23]L. L. Zhao, T. Yi, J. C. Fettinger, S. M. Kauzlarich, and E. Morosan, Phys. Rev. B **80**, 020404(R) (2009).
[24]T. Yi, A. P. Dioguardi, P. Klavins, N. J. Curro, L. L. Zhao, E. Morosan, and S. M. Kauzlarich, Eur. J. Inorg. Chem (submitted May 2011), doi: 10.1002/ejic.201100349.
[25]M. Rotter, M. Tegel, D. Johrendt, I. Schellenberg, W. Hermes, and R. Pöttgen, Phys. Rev. B **78**, 020503(R) (2008).
[26]Y. Nambu, L. L. Zhao, E. Morosan, K. Kim, G. Kotliar, P. Zajdel, M. A. Green, W. Ratcliff, J. A. Rodriguez-Rivera, and C. Broholm, Phys. Rev. Lett. **106**, 037201 (2011).
[27]P. C. Canfield and S. L. Bud'ko, Ann. Rev. Condens. Matter Phys. **1**, 27 (2010).
[28]M. Rotter, M. Pangerl, M. Tegel, and D. Johrendt, Angew. Chem. **47**, 7949 (2008).
[29]N. Ni, M. E. Tillman, J.-Q. Yan, A. Kracher, S. T. Hannahs, S. L. Bud'ko, and P. C. Canfield, Phys. Rev. B **78**, 214515 (2008).
[30]S. Jiang, H. Xing, G. Xuan, C. Wang, Z. Ren, C. Feng, J. Dai, Z. Xu, and G. Cao, J. Phys. Condens. Matter **21**, 382203 (2009).
[31]X. H. Chen, T. Wu, G. Wu, R. H. Liu, H. Chen, and D. F. Fang, Nature **453**, 761 (2008).
[32]H. Takahashi, K. Igawa, K. Arii, Y. Kamihara, M. Hirano, and H. Hosono, Nature **453**, 376 (2008).
[33]P. L. Alireza, Y. T. C. Ko, J. Gillett, C. M. Petrone, J. M. Cole, G. G. Lonzarich, and S. E. Sebastian, J. Phys. Condens. Matter **21**, 012208 (2009).
[34]E. Colombier, S. L. Bud'ko, N. Ni, and P. C. Canfield, Phys. Rev. B **79**, 224518 (2009).
[35]F. Ishikawa, N. Eguchi, M. Kodama, K. Fujimaki, M. Einaga, A. Ohmura, A. Nakayama, A. Mitsuda, and Y. Yamada, Phys. Rev. B **79**, 172506 (2009).
[36]H. Fukazawa, N. Takeshita, T. Yamazaki, K. Kondo, K. Hirayama, Y. Kohori, K. Miyazawa, H. Kito, H. Eisaki, and A. Iyo, J. Phys. Soc. Jpn. **77**, 105004 (2008).
[37]P. Manuel, L. C. Chapon, I. S. Todorov, D. Y. Chung, J.-P. Castellan, S. Rosenkranz, R. Osborn, P. Toledano, and M. G. Kanatzidis, Phys. Rev. B **81**, 184402 (2010).
[38]L. J. Farrugia, J. Appl. Crystallogr. **32**, 837 (1999).
[39]A. Altomare, M. C. Burla, M. Camalli, G. L. Cascarano, C. Giacovazzo, A. Guagliardi, A. G. G. Moliterni, G. Polidori, and R. Spagna, J. Appl. Crystallogr. **32**, 115 (1999).
[40]G. M. Sheldrick, Acta Crystallogr. Sect. A **64**, 112 (2008).
[41]A. L. Spek, J. Appl. Crystallogr. **36**, 7 (2003).
[42]E. Colombier and D. Braithwaite, Rev. Sci. Instrum. **78**, 093903 (2007).
[43]J. P. S. Klotz and E. Cochard, J. Phys. D: Appl. Phys. **39**, 1674 (2006).
[44]S. K. Kim (unpublished).
[45]R. Klingeler, N. Leps, I. Hellmann, A. Popa, U. Stockert, C. Hess, V. Kataev, H.-J. Grafe, F. Hammerath, G. Lang, S. Wurmehl, G. Behr, L. Harnagea, S. Singh, and B. Büchner, Phys. Rev. B **81**, 024506 (2010).
[46]G. Wu, H. Chen, T. Wu, Y. L. Xie, Y. J. Yan, R. H. Liu, X. F. Wang, J. J. Ying, and X. H. Chen, J. Phys. Condens. Matter **20**, 422201 (2008).
[47]N. Ni, S. Nandi, A. Kreyssig, A. I. Goldman, E. D. Mun, S. L. Bud'ko, and P. C. Canfield, Phys. Rev. B **78**, 014523 (2008).
[48]J.-Q. Yan, A. Kreyssig, S. Nandi, N. Ni, S. L. Bud'ko, A. Kracher, R. J. McQueeney, R. W. McCallum, T. A. Lograsso, A. I. Goldman, and P. C. Canfield, Phys. Rev. B **78**, 024516 (2008).
[49]X. F. Wang, T. Wu, G. Wu, H. Chen, Y. L. Xie, J. J. Ying, Y. J. Yan, R. H. Liu, and X. H. Chen, Phys. Rev. Lett. **102**, 117005 (2009).
[50]G. M. Zhang, Y. H. Su, Z. Y. Lu, Z. Y. Weng, D. H. Lee, and T. Xiang, Europhys. Lett. **86**, 37006 (2009).
[51]R. Klingeler, N. Leps, I. Hellmann, A. Popa, U. Stockert, C. Hess, V. Kataev, H.-J. Grafe, F. Hammerath, G. Lang, S. Wurmehl, G. Behr, L. Harnagea, S. Singh, and B. Büchner, Phys. Rev. B **81**, 024506 (2010).
[52]G. LeBras, Z. Konstantinovic, D. Colson, A. Forget, J.-P. Carton, C. Ayache, F. Jean, G. Collin, and Y. Dumont, Phys. Rev. B **66**, 174517 (2002).
[53]R. D. Shannon, Acta Crystallogr. Sect. A **32**, 751 (1976).
[54]I. Todorov, D. Y. Chung, H. Claus, K. E. Gray, Q. Li, J. Schleuter, T. Bakas, A. P. Douvalis, M. Gutmann, and M. G. Kanatzidis, Chem. Mater. **22**, 4996 (2010).
[55]N. Ni, A. Thaler, J. Q. Yan, A. Kracher, E. Colombier, S. L. Bud'ko, P. C. Canfield, and S. T. Hannahs, Phys. Rev. B **82**, 024519 (2010).
[56]J.-E. Jørgensen, J. S. Olsen, and L. Gerward, Solid State Commun. **149**, 1161 (2009).
[57]M. S. Kim, Z. P. Yin, L. L. Zhao, E. Morosan, G. Kotliar, and M. C. Aronson, Phys. Rev. B **84**, 075112 (2011).